

## Direct measurement of terahertz conductivity in a gated monolayer semiconductor

Su-Di Chen<sup>1,2,3</sup>, Qixin Feng<sup>1,3</sup>, Wenyu Zhao<sup>1</sup>, Ruishi Qi<sup>1</sup>, Zuocheng Zhang<sup>1</sup>, Dishan Abeysinghe<sup>1,3</sup>, Can Uzundal<sup>1,3,4</sup>, Jingxu Xie<sup>3,5</sup>, Takashi Taniguchi<sup>6</sup>, Kenji Watanabe<sup>7</sup>, Feng Wang<sup>1,2,3,\*</sup>

<sup>1</sup> Department of Physics, University of California, Berkeley, CA 94720, USA.

<sup>2</sup> Kavli Energy NanoSciences Institute, University of California Berkeley and Lawrence Berkeley National Laboratory, Berkeley, CA 94720, USA.

<sup>3</sup> Materials Sciences Division, Lawrence Berkeley National Laboratory, Berkeley, CA 94720, USA.

<sup>4</sup> Department of Chemistry, University of California, Berkeley, CA 94720, USA.

<sup>5</sup> Graduate Group in Applied Science and Technology, University of California, Berkeley, CA 94720, USA.

<sup>6</sup> Research Center for Materials Nanoarchitectonics, National Institute for Materials Science, 1-1 Namiki, Tsukuba 305-0044, Japan.

<sup>7</sup> Research Center for Electronic and Optical Materials, National Institute for Materials Science, 1-1 Namiki, Tsukuba 305-0044, Japan.

\* To whom correspondence should be addressed: fengwang76@berkeley.edu

**Abstract:** Two-dimensional semiconductors and their moiré superlattices have emerged as important platforms for investigating correlated electrons. However, many key properties of these systems, such as the frequency-dependent conductivity, remain experimentally inaccessible because of the mesoscopic sample size. Here we report a technique to directly measure the complex conductivity of electrostatically gated two-dimensional semiconductors in the terahertz frequency range. Applying this technique to a WSe<sub>2</sub> monolayer encapsulated in hBN, we observe clear Drude-like response between 0.1 and 1 THz, in a density range challenging to access even in DC transport. Our work opens a new avenue for studying tunable van der Waals heterostructures using terahertz spectroscopy.

**Main text:** Conductivity as a function of frequency is a key observable in solids, encoding rich information about the underlying electronic states [1]. In correlated electron systems, conductivity in the terahertz (THz) frequency range is of particular interest because of its overlap with emergent energy scales from quasiparticle scattering rates in metals to energy gaps and collective modes in broken-symmetry states [2–5]. Experimentally, THz spectroscopy, a direct probe of THz conductivity, has played vital roles in the study of correlated states hosted by bulk materials and large thin films. However, its application to van der Waals heterostructures, a rising platform [6–10] featuring exceptional tunability from mechanical stacking and electrostatic gating, has been challenging. First, the size of the vdW heterostructures, typically around tens of microns, is much smaller than the wavelength of the THz photons on the order of hundreds of microns. This length-scale mismatch necessitates near-field approaches [11–14], through which to extract quantitatively the conductivity spectra is often difficult. Moreover, as the sample and

the gate electrode are arranged in a parallel-plate-capacitor geometry, it is hard to separate the THz response of the sample from that of the gate material.

On-chip THz spectroscopy is an emerging technique that partially resolves these challenges [15–19]. In this technique, the sample interacts with THz fields confined in waveguides. If the sample is conducting enough, simple circuit models can be used to convert the measured waveguide transmission to sample conductivity [15]. Background contributions from the gate electrode can also be ignored, if its conductance is much lower than that of the sample. Because of these constraints, absolute measurement of THz conductivity in a vdW heterostructure has only been accomplished in graphene at high dopings, using a much-less-conducting transition metal dichalcogenide (TMD) as gate [15]. In this work, we will demonstrate THz conductivity measurement on gated monolayer TMD for the first time. By introducing an improved waveguide design, a new gate material, and a new analysis protocol, our work opens up possibilities for the THz study of generic vdW heterostructures.

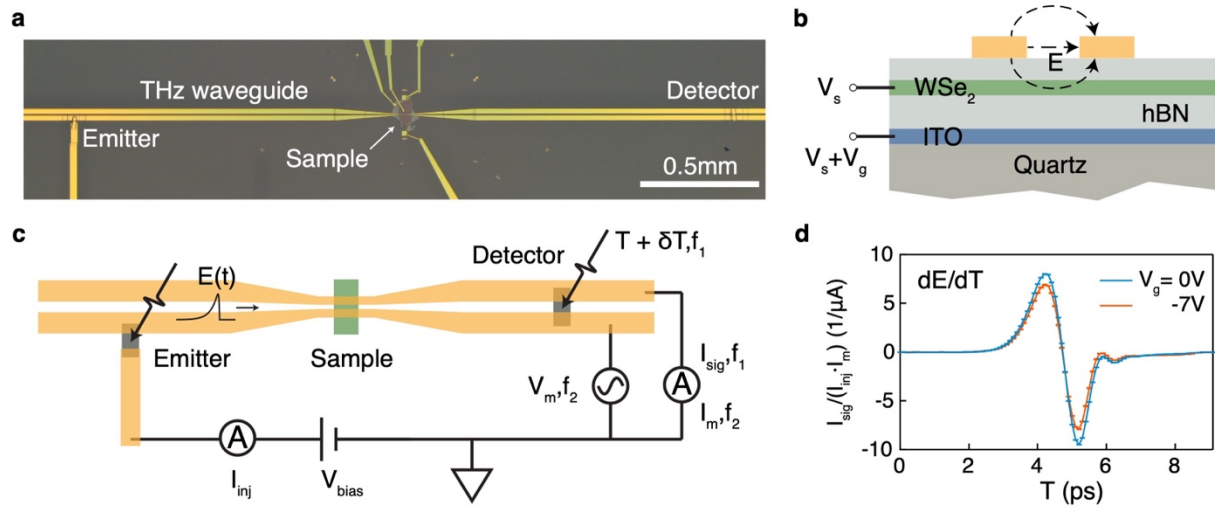


Fig. 1. Terahertz (THz) time-domain spectroscopy inside an on-chip waveguide. **a.** Microscope photograph of the center part of the device for THz spectroscopy. **b.** Schematic cross-sectional view of the sample segment in **a** perpendicular to the THz propagation direction. The monolayer WSe<sub>2</sub> sample is gated by a 5-nm-thick indium tin oxide (ITO) electrode across a 73-nm-thick hexagonal boron nitride (hBN) dielectric layer. **c.** Schematics of the measurement circuit. Pulsed THz fields ( $E$ ) with few-ps duration are generated at 80 MHz repetition rate by a laser-excited photoconductive switch (emitter), and after interacting with the sample, sampled at different time delays ( $T$ ) by a second switch (detector).  $T$  is modulated by  $\delta T = 0.17$  ps at  $f_1 = 50$  Hz, and a small AC monitoring voltage  $V_m$  is applied between the waveguide traces at  $f_2 = 127$  Hz. In-phase photocurrents across the detector at  $f_1$  (denoted  $I_{\text{sig}}$ ) and  $f_2$  (denoted  $I_m$ ), and the average photocurrent injected through the emitter ( $I_{\text{inj}}$ ) are measured. **d.** Normalized signal  $I_{\text{sig}}/I_{\text{inj}} \cdot I_m$ , which is proportional to  $dE/dT$  of the transmitted pulse convolved with the detector time resolution, as a function of  $T$  for undoped (gate voltage  $V_g = 0$  V) and hole-doped WSe<sub>2</sub> ( $V_g = -7$  V). Error bars represent 1- $\sigma$  noise in measurement.

The layout of our device is shown in Figs. 1a and b (see also Fig. S1). The topmost layer of the structure is a gold coplanar stripline (CPS) waveguide [20] with integrated photoconductive switches made of low-temperature-grown GaAs [2]. Broadband THz pulses are injected into the CPS by exciting the biased emitter switch with a femtosecond laser pulse. The transmitted THz electric field is then sampled in the time domain by the detector switch triggered with a second laser pulse. The total length of the CPS is 8.5 mm, with the emitter and detector placed at its trisecting points. This arrangement ensures that the directly transmitted signal, which we collect and analyze, is separated in time from those reflected by the switches and the CPS terminations.

Near the center of the CPS, the width of and gap between the metal traces are gradually narrowed to 2.26 and 0.49  $\mu\text{m}$ , respectively. The sample, a monolayer WSe<sub>2</sub> flake encapsulated in hexagonal boron nitride (hBN), sits right beneath the narrowest segment. This tapered design enhances the THz field in the sample, and thus the sensitivity of the measurement. Moreover, it allows the contacts and the edge of the flake to be placed at distances much larger than the CPS dimension perpendicular to the propagation direction, effectively eliminating their interference with the waveguide mode.

The sample is charge neutral and insulating at low temperature. We define an active region smaller than the WSe<sub>2</sub> flake using a rectangular-shaped backgate 20- $\mu\text{m}$  wide along the propagation direction (see supplementary materials section 1 for details). The gate electrode is made of indium tin oxide (ITO), an electron-doped semiconductor, with a thickness around 5 nm. Through DC transport measurements, we determine its sheet conductance ( $\sigma_{\text{ITO}}$ ) and mobility ( $\mu_{\text{ITO}}$ ) to be around 0.11 mS and 40  $\text{cm}^2\text{V}^{-1}\text{s}^{-1}$ , respectively (see supplementary materials section 4 for details). These properties are ideal for our measurements. First, assuming an electron effective mass of  $0.3m_0$  [21],  $\mu_{\text{ITO}}$  translates to a transport scattering time  $\tau_{\text{ITO}} \approx 7$  fs. Thus, below a few THz,  $\sigma_{\text{ITO}}$  can essentially be treated as frequency independent, simplifying the modeling of the structure. Moreover,  $\sigma_{\text{ITO}}$  is small enough, such that the gate electrode does not strongly reflect or screen the THz field which needs to interact with the sample. In addition, the electron density in ITO is estimated to be  $n_{\text{ITO}} \approx \sigma_{\text{ITO}}/e\mu_{\text{ITO}} \approx 1.7 \times 10^{13} \text{ cm}^{-2}$ , which sets a generous upper bound for the maximal achievable electron density in the sample through gating (the hole density is not limited). Here  $e$  denotes the elementary charge.

We illustrate our measurement circuits in Fig. 1c. A femtosecond laser is used to excite first the emitter and after a time delay  $T$  the detector, at a repetition rate of 80 MHz. The emitter is biased at  $V_{\text{bias}} = 7.6$  V using a source meter, which also measures the average photocurrent injected into the CPS,  $I_{\text{inj}}$  (around 80 nA). The photocurrent through the detector, which is proportional to the transient transmitted electric field  $E(T)$  convolved with the time resolution of detection, is collected by a current preamplifier. To reduce noise, we modulate  $T$  with an amplitude of 0.17 ps at  $f_1 = 50$  Hz, and read out the resulting modulation in photocurrent  $I_{\text{sig}}$  using a lock-in amplifier, effectively measuring  $dE(T)/dT$ . In addition, we apply a small AC voltage,  $V_m = 2$  mV at  $f_2 = 127$  Hz, between the waveguide traces and monitor the resulting in-phase detector photocurrent  $I_m$  using a second lock-in amplifier. As the photoconductances of the emitter and detector are

sensitive to drifts in laser power and beam positions, we normalize  $I_{\text{sig}}$  by  $I_{\text{inj}} \cdot I_{\text{m}}$  to remove extrinsic drifts from the signal.

During measurements, we change the gate voltage  $V_g$  between the sample and the ITO to access different doping states. We also set the voltage difference between the sample and the waveguide to  $V_s = -0.2$  V, to align the hole density underneath the metal traces with the rest of the gated region (see supplementary materials section 4 for details). Two representative time domain traces of  $I_{\text{sig}} / (I_{\text{inj}} \cdot I_{\text{m}})$  measured at 20 K are shown in Fig. 1d, at  $V_g = 0$  V (WSe<sub>2</sub> undoped) and -7 V (WSe<sub>2</sub> hole-doped). Because  $I_{\text{sig}} / (I_{\text{inj}} \cdot I_{\text{m}}) = C_0 \cdot dE/dT \otimes R$ , where  $C_0$  is a constant and  $R$  represents the finite resolution of detection, after Fourier transform (FT) we obtain  $t/t_0 = \text{FT}[I_{\text{sig}} / (I_{\text{inj}} \cdot I_{\text{m}})] / \text{FT}[I_{\text{sig}} / (I_{\text{inj}} \cdot I_{\text{m}})]_{V_g = 0\text{V}}$  in the frequency domain, where  $t(t_0)$  is the field transmission coefficient in the doped (undoped) state.

We plot the amplitude and phase of  $t/t_0$  as functions of frequency in Figs. 2f and g, respectively. The remaining task is to convert  $t/t_0$  to the conductivity  $\sigma = \sigma_1 + i\sigma_2$  of doped holes. Instead of using approximate analytical formulas, we numerically obtain the mapping between  $t/t_0$  and  $\sigma$ . First, we discretize the CPS into a large number of segments (Fig. 2a) where each segment has its own cross-sectional geometry. We have characterized the actual geometries using optical microscopy, scanning electron microscopy (SEM), and atomic force microscopy (AFM) to ensure the accuracy of modeling. For each segment at every frequency, we solve the two-dimensional waveguide mode numerically (see Figs. 2b and c for example, see also supplementary materials section 7 for more details) and obtain its effective refractive index  $n_{\text{eff}}$  and characteristic impedance  $Z_0$ . In particular for the sample segment, we solve the mode on a parameter grid spanned by different  $\sigma_1$  and  $\sigma_2$  values while setting  $\sigma_{\text{ITO}}$  to its experimentally measured value at  $V_g = 0$  V. With all  $n_{\text{eff}}$  and  $Z_0$  known, we then use a transfer matrix calculation [22] to determine the waveguide transmission  $t$  as a function of  $\sigma_1$  and  $\sigma_2$ . This is analogous to calculating the optical transmission through a multilayer medium, although here in the CPS each segment is parameterized by both  $n_{\text{eff}}$  and  $Z_0$ , instead of a single refractive index.

Using these calculations, we can obtain  $t/t_0 = t(\sigma)/t(\sigma=0)$  on a grid in the complex plane of  $\sigma$  at every frequency (see Figs. 2d and e for an example at 0.5 THz). Within the relevant  $\sigma$  range, both

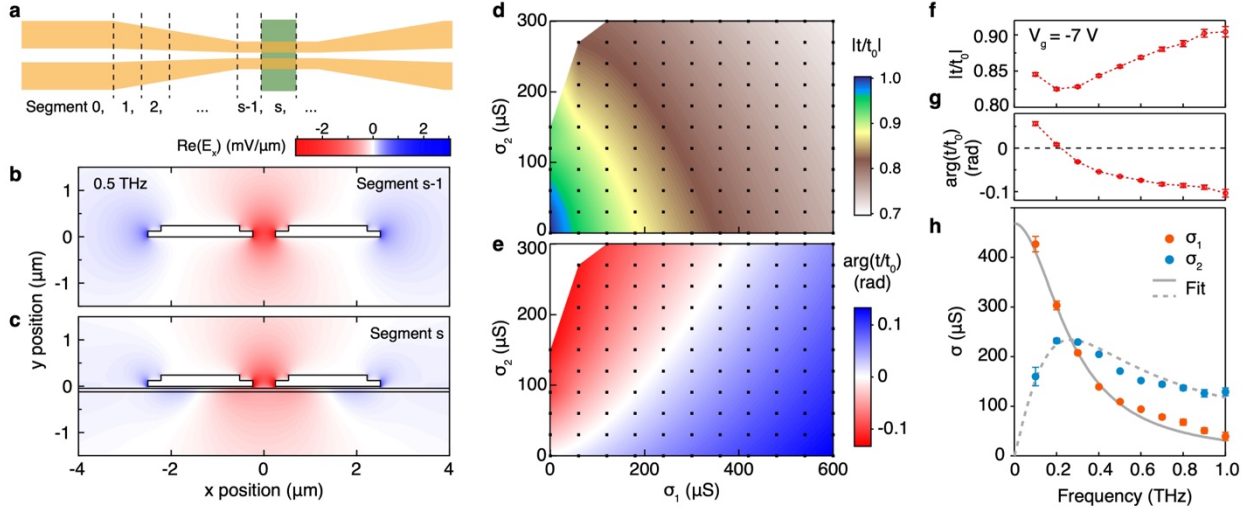


Fig. 2. Extract conductivity from experiment. **a**. Schematic of waveguide modeling. The structure is discretized into many segments. The waveguide mode is numerically solved for each segment, allowing the total transmission to be calculated using transfer matrix method. The actual segment interval is  $0.5 \mu\text{m}$  in the tapered section, which is exaggerated in the schematic for clarity. **b**. Cross-sectional mode profile at  $0.5 \text{ THz}$  in segment  $s-1$ , near the metal traces outlined in black. The color scale represents the in-phase component of electric field along the horizontal direction and is oversaturated for clarity. Data are normalized such that the voltage difference between the metal traces equal to  $1 \text{ mV}$ . **c**. Same as **b** for segment  $s$ . The horizontal lines mark the  $\text{WSe}_2$  (top) and  $\text{ITO}$  (bottom) layers, with their sheet conductance at  $300+300i \mu\text{S}$  and  $109 \mu\text{S}$ , respectively. **d**. Amplitude of the transmission coefficient  $t$  at  $0.5 \text{ THz}$  as a function of the real ( $\sigma_1$ ) and imaginary ( $\sigma_2$ ) parts of sample conductance normalized by that at  $\sigma_1=\sigma_2=0$  ( $t_0$ ). Actual simulations are performed on the grid marked by black dots and the color plot is a Voronoi interpolation of the simulations. **e**. same as **d** for the phase shift  $\arg(t/t_0)$ . **f**. Frequency evolution of  $|t/t_0|$  obtained from measured data in Fig. 1d, using the undoped trace as reference. **g**. same as **f** for  $\arg(t/t_0)$ . **h**. Sample conductivity extracted from data in **f** and **g**, using simulated mappings at 10 frequencies. A simultaneous Drude fit to both the real and imaginary parts are plotted in grey. Error bars in **f**, **g**, and **h** represent  $1-\sigma$  error from noise in measurements.

the amplitude and phase of  $t/t_0$  evolve in a nearly monotonic fashion, with their constant-value contour lines following distinct directions. This indicates a one-to-one correspondence between  $t/t_0$  and  $\sigma$ . We can thus convert the experimentally measured data to conductivity using the simulated mapping. As a remark, we have ignored the change of  $\sigma_{\text{ITO}}$  with  $V_g$  in this analysis because  $\mu_{\text{ITO}}$  is much smaller than the mobility of  $\text{WSe}_2$  within the measured frequency range. If needed, one can also take this effect into account by calculating the conversion mapping using the measured  $\sigma_{\text{ITO}}$  values at each  $V_g$  instead (see supplementary materials section 5).

The converted results from  $V_g = -7 \text{ V}$  are plotted in Fig. 2h. We observe a clear drop of  $\sigma_1$  with increasing frequency, and a non-monotonic  $\sigma_2$  that crosses  $\sigma_1$  near  $0.3 \text{ THz}$ . We fit both curves simultaneously using a Drude model with frequency-independent scattering time:  $\sigma = \frac{D}{\pi} \frac{1}{1/\tau - if/2\pi}$ . Here the only fitting parameters are  $D$  and  $\tau$ , which denote the Drude weight and the

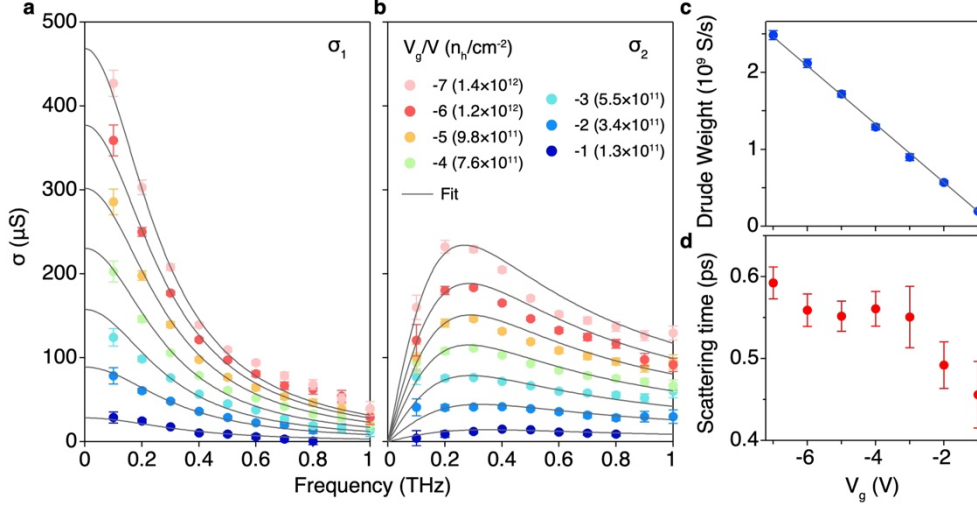


Fig. 3. Doping evolution of conductivity spectra. **a**, **b**, real and imaginary parts of WSe<sub>2</sub> conductance as functions of frequency at various  $V_g$  (labeled in **b** in units of V). The corresponding hole densities  $n_h$  are calculated using a parallel-plate-capacitor model and provided in parentheses in units of  $\text{cm}^{-2}$ . For each  $V_g$ , data from both panels are fit to the Drude expression and the results are plotted in grey. Error bars in **a** and **b** represent 1- $\sigma$  error from noise in measurements. **c**. Drude weight extracted from the fitting in **a** and **b** as a function of  $V_g$ . A linear fit to the data is plotted in grey. **d**. Same as **c** for the scattering time. Error bars in **c** and **d** represent 1- $\sigma$  error from fitting.

scattering time, respectively. We obtain  $D = 2.48(6) \times 10^9$  S/s and  $\tau = 0.59(2)$  ps. The fitting results are plotted in grey, which well reproduce the data.

We show the doping evolution of  $\sigma$  in Fig. 3. All data are measured at 20 K, the base temperature of our cryostat. We determine the hole density as  $n_h = \epsilon_0 \epsilon_r (V_g - V_0) / de$ , where  $\epsilon_0$  is the vacuum permittivity,  $\epsilon_r = 2.8$  is the DC dielectric constant of hBN along the out-of-plane direction,  $V_0 = -0.4$  V is the onset gate voltage of hole doping, and  $d = 73$  nm is the thickness of the hBN dielectric measured by AFM. Here  $V_0$  is determined using optical and ITO sensing methods on the same device, and  $\epsilon_r$  is measured on another hBN flake exfoliated from the same batch of hBN crystals (see supplementary materials sections 3, 4, and 6 for details). We observe that the conductivity below 1 THz in the density range between  $1.3 \times 10^{11}$  and  $1.4 \times 10^{12} \text{ cm}^{-2}$  well follows a canonical Drude form. The Drude weight is found to evolve linearly as a function of  $V_g$  (Fig. 4d), which indicates a constant effective mass in the measured doping range. A linear fit to the data extrapolates to 0 at  $V_g = -0.5$  V, consistent with  $V_0$  within experimental uncertainties. From the slope of the fit, we obtain a hole effective mass  $m^* = \pi e^2 (dD/dn_h)^{-1} = 0.50 \pm 0.09 m_0$ , where  $m_0$  is the bare electron mass and the uncertainty mostly originates from that in  $n_h$ . This is close to values reported in previous quantum oscillation measurements [23,24], and agrees with band structures measured by angle-resolved photoemission spectroscopy without magnetic fields [25].

Fig. 3d shows the extracted scattering time, which gradually reduces from 0.59(2) ps at  $V_g = -7$  V to 0.46(4) ps at -1 V. These values correspond to mobilities of  $2.1 \times 10^3$  and  $1.6 \times 10^3 \text{ cm}^2 \text{ V}^{-1} \text{ s}^{-1}$  at  $n_h = 1.4 \times 10^{12}$  and  $1.3 \times 10^{11} \text{ cm}^{-2}$ , respectively. Remarkably, DC transport measurements in this

density range have only become possible very recently, after the development of low-resistance charge-transfer contacts [26,27]. Although the absolute mobility values observed here are lower than those reported by Park et al. in their flux-grown samples [26], the qualitative density dependence is consistent and suggests the enhanced role of impurity scattering with decreasing carrier density.

To conclude, our data provide the first experimental confirmation of the Drude frequency response in an electrostatically gated semiconductor. Moreover, they validate the experimental methods developed for directly measuring THz conductivity in mesoscopic gated devices. Our work lays the foundation for investigating various correlated electronic states in vdW heterostructures using THz spectroscopy.

### **Data availability**

The data that support the findings of this study are available from the corresponding author upon reasonable request.

### **Acknowledgement**

We thank A. Y. Joe for discussions. The THz measurement was supported by the NSF award no. 2311205. The device fabrication was supported by the U.S. Department of Energy, Office of Science, Office of Basic Energy Sciences, Materials Sciences and Engineering Division under contract no. DE-AC02-05-CH11231 (van der Waals heterostructures program, KCWF16). The simulations were performed at the Molecular Graphics and Computation Facility (MGCF) at UC Berkeley and the MGCF is in part supported by NIH S10OD034382. K.W. and T.T. acknowledge support from the Japan Society for the Promotion of Science (KAKENHI grants 21H05233 and 23H02052) and the World Premier International Research Center Initiative, Ministry of Education, Culture, Sports, Science and Technology, Japan. R.Q. acknowledges support from the Kavli ENSI Graduate Student Fellowship. S.D.C. acknowledges support from the Kavli ENSI Heising-Simons Junior Fellowship.

### **Author contributions**

F.W. and S.D.C. proposed the experiment; S.D.C. fabricated the devices with help from Q.F., W.Z., R.Q., Z.Z., D.A., and J.X.; S.D.C. built the experimental setup and collected the data with help from W.Z., C.U., and D.A.; S.D.C. performed the simulations and analyzed the data; T.T. and K.W. grew the hBN crystals; S.D.C. and F.W. wrote the manuscript; F.W. supervised the project.

### **Competing interest**

The authors declare no competing interests.

### **References**

- [1] M. Dressel and G. Grüner, *Electrodynamics of Solids: Optical Properties of Electrons in Matter* (Cambridge University Press, Cambridge, 2002).
- [2] M. C. Nuss and J. Orenstein, *Terahertz Time-Domain Spectroscopy*, in *Millimeter and Submillimeter Wave Spectroscopy of Solids*, edited by G. Grüner (Springer, Berlin, Heidelberg, 1998), pp. 7–50.
- [3] R. Ulbricht, E. Hendry, J. Shan, T. F. Heinz, and M. Bonn, Carrier dynamics in semiconductors studied with time-resolved terahertz spectroscopy, *Rev. Mod. Phys.* 83, 543 (2011).
- [4] D. N. Basov, R. D. Averitt, D. van der Marel, M. Dressel, and K. Haule, *Electrodynamics of correlated electron materials*, *Rev. Mod. Phys.* 83, 471 (2011).
- [5] N. P. Armitage, *Electrodynamics of Correlated Electron Systems*, arXiv:0908.1126.
- [6] A. K. Geim and I. V. Grigorieva, Van der Waals heterostructures, *Nature* 499, 419 (2013).
- [7] L. Balents, C. R. Dean, D. K. Efetov, and A. F. Young, Superconductivity and strong correlations in moiré flat bands, *Nat. Phys.* 16, 725 (2020).
- [8] D. M. Kennes, M. Claassen, L. Xian, A. Georges, A. J. Millis, J. Hone, C. R. Dean, D. N. Basov, A. N. Pasupathy, and A. Rubio, Moiré heterostructures as a condensed-matter quantum simulator, *Nat. Phys.* 17, 155 (2021).
- [9] K. F. Mak and J. Shan, Semiconductor moiré materials, *Nat. Nanotechnol.* 17, 686 (2022).
- [10] L. Ju, A. H. MacDonald, K. F. Mak, J. Shan, and X. Xu, The fractional quantum anomalous Hall effect, *Nat. Rev. Mater.* 9, 455 (2024).
- [11] L. Novotny and B. Hecht, *Principles of Nano-Optics*, 2nd ed. (Cambridge University Press, Cambridge, 2012).
- [12] J. Zhang, X. Chen, S. Mills, T. Ciavatti, Z. Yao, R. Mescall, H. Hu, V. Semenenko, Z. Fei, H. Li, V. Perebeinos, H. Tao, Q. Dai, X. Du, and M. Liu, Terahertz Nanoimaging of Graphene, *ACS Photonics* 5, 2645 (2018).
- [13] R. Jing, Y. Shao, Z. Fei, C. F. B. Lo, R. A. Vitalone, F. L. Ruta, J. Staunton, W. J.-C. Zheng, A. S. Mcleod, Z. Sun, B. Jiang, X. Chen, M. M. Fogler, A. J. Millis, M. Liu, D. H. Cobden, X. Xu, and D. N. Basov, Terahertz response of monolayer and few-layer WTe<sub>2</sub> at the nanoscale, *Nat. Commun.* 12, 5594 (2021).
- [14] X. Guo, K. Bertling, B. C. Donose, M. Brünig, A. Cernescu, A. A. Govyadinov, and A. D. Rakić, Terahertz nanoscopy: Advances, challenges, and the road ahead, *Appl. Phys. Rev.* 11, 021306 (2024).
- [15] P. Gallagher, C.-S. Yang, T. Lyu, F. Tian, R. Kou, H. Zhang, K. Watanabe, T. Taniguchi, and F. Wang, Quantum-critical conductivity of the Dirac fluid in graphene, *Science* 364, 158 (2019).
- [16] W. Zhao, S. Wang, S. Chen, Z. Zhang, K. Watanabe, T. Taniguchi, A. Zettl, and F. Wang, Observation of hydrodynamic plasmons and energy waves in graphene, *Nature* 614, 688 (2023).
- [17] J. W. McIver, B. Schulte, F.-U. Stein, T. Matsuyama, G. Jotzu, G. Meier, and A. Cavalleri, Light-induced anomalous Hall effect in graphene, *Nat. Phys.* 16, 38 (2020).
- [18] G. Kipp, H. M. Bretscher, B. Schulte, D. Herrmann, K. Kusyak, M. W. Day, S. Kesavan, T. Matsuyama, X. Li, S. M. Langner, J. Hagelstein, F. Sturm, A. M. Potts, C. J. Eckhardt, Y. Huang, K. Watanabe, T. Taniguchi, A. Rubio, D. M. Kennes, M. A. Sentef, E. Baudin, G. Meier, M. H. Michael, and J. W. McIver, Cavity Electrodynamics of van Der Waals Heterostructures, arXiv:2403.19745.



- [19] A. M. Potts, A. K. Nayak, M. Nagel, K. Kaj, B. Stamenic, D. D. John, R. D. Averitt, and A. F. Young, On-Chip Time-Domain Terahertz Spectroscopy of Superconducting Films below the Diffraction Limit, *Nano Lett.* 23, 3835 (2023).
- [20] D. R. Grischkowsky, Optoelectronic characterization of transmission lines and waveguides by terahertz time-domain spectroscopy, *IEEE J. Sel. Top. Quantum Electron.* 6, 1122 (2000).
- [21] Y. Ohhata, F. Shinoki, and S. Yoshida, Optical properties of r.f. reactive sputtered tin-doped In<sub>2</sub>O<sub>3</sub> films, *Thin Solid Films* 59, 255 (1979).
- [22] D. M. Pozar, *Microwave Engineering*, 4th Edition (Wiley, 2011).
- [23] B. Fallahazad, H. C. P. Movva, K. Kim, S. Larentis, T. Taniguchi, K. Watanabe, S. K. Banerjee, and E. Tutuc, Shubnikov--de Haas Oscillations of High-Mobility Holes in Monolayer and Bilayer WSe<sub>2</sub>: Landau Level Degeneracy, Effective Mass, and Negative Compressibility, *Phys. Rev. Lett.* 116, 086601 (2016).
- [24] A. Y. Joe, K. Pistunova, K. Kaasbjerg, K. Wang, B. Kim, D. A. Rhodes, T. Taniguchi, K. Watanabe, J. Hone, T. Low, L. A. Jauregui, and P. Kim, Transport Study of Charge-Carrier Scattering in Monolayer WSe<sub>2</sub>, *Phys. Rev. Lett.* 132, 056303 (2024).
- [25] Y. Zhang, M. M. Ugeda, C. Jin, S.-F. Shi, A. J. Bradley, A. Martín-Recio, H. Ryu, J. Kim, S. Tang, Y. Kim, B. Zhou, C. Hwang, Y. Chen, F. Wang, M. F. Crommie, Z. Hussain, Z.-X. Shen, and S.-K. Mo, Electronic Structure, Surface Doping, and Optical Response in Epitaxial WSe<sub>2</sub> Thin Films, *Nano Lett.* 16, 2485 (2016).
- [26] J. Pack, Y. Guo, Z. Liu, B. S. Jessen, L. Holtzman, S. Liu, M. Cothrine, K. Watanabe, T. Taniguchi, D. G. Mandrus, K. Barmak, J. Hone, and C. R. Dean, Charge-transfer contacts for the measurement of correlated states in high-mobility WSe<sub>2</sub>, *Nat. Nanotechnol.* 19, 948 (2024).
- [27] J. Xie, Z. Zhang, H. Zhang, V. Nagarajan, W. Zhao, H.-L. Kim, C. Sanborn, R. Qi, S. Chen, S. Kahn, K. Watanabe, T. Taniguchi, A. Zettl, M. F. Crommie, J. Analytis, and F. Wang, Low Resistance Contact to P-Type Monolayer WSe<sub>2</sub>, *Nano Lett.* 24, 5937 (2024).

## Supplementary materials for

### “Direct measurement of terahertz conductivity in a gated monolayer semiconductor”

#### 1. Device fabrication

We start from a 500- $\mu\text{m}$ -thick Z-cut quartz substrate, chosen for its minimal THz absorption. Using photolithography followed by magnetron sputtering at room temperature, we first deposit a 5-nm-thick ITO gate electrode (Fig. S1, dashed rectangle) onto the substrate. After liftoff, we anneal the as-grown ITO at 250 °C for 2 minutes in a nitrogen environment to improve its stability.

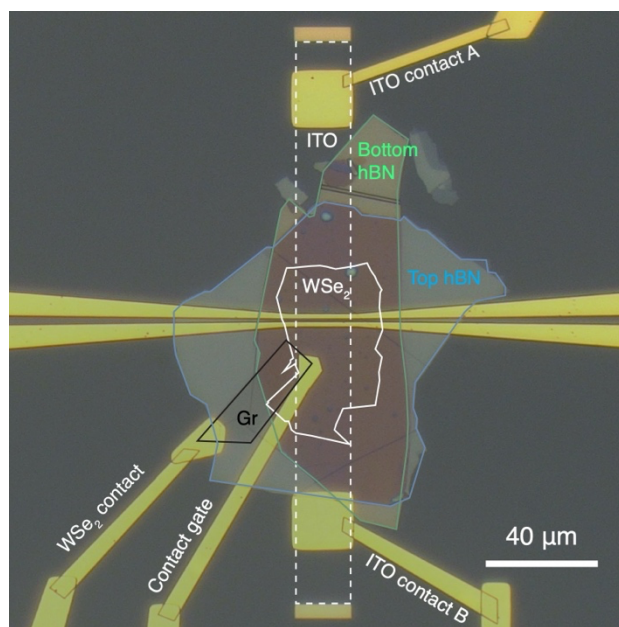


Fig. S1. Microscope photograph of central part of the device near the WSe<sub>2</sub> sample. The blue, solid white, black, green, and dashed white lines mark the boundaries of top hBN (43-nm thickness), monolayer WSe<sub>2</sub>, few-layer graphite (Gr), bottom hBN (73-nm thickness), and ITO (5-nm thickness), respectively. The two-terminal resistance of ITO is measured between ITO contacts A and B, which are separated by 130  $\mu\text{m}$ . The overlap between WSe<sub>2</sub> and ITO is approximately 56  $\mu\text{m}$  along the vertical direction of the photograph.

Separately, we exfoliate WSe<sub>2</sub> (HQ graphene), hBN, and graphite flakes onto SiO<sub>2</sub>/Si substrates. Using a Bisphenol-A polycarbonate (PC) stamp, we pick up the top hBN (43-nm thickness), monolayer WSe<sub>2</sub>, few-layer graphite (Gr, used as contact to WSe<sub>2</sub>), and bottom hBN (73-nm thickness) flakes sequentially at around 75 °C. The assembled stack is then released onto the ITO gate electrode at 180 °C. Afterwards, the PC residue is dissolved in chloroform at room temperature. The chip is cleaned in acetone, isopropanol, and deionized water, before dried under nitrogen flow. The hBN thicknesses are determined using AFM after completion of the device.

With the stack in position, we use photolithography and electron-beam evaporation to define the contacts to Gr and ITO, as well as the wide sections of the CPS waveguide away from the sample and the photoconductive switches. 90 nm of Au is deposited in this step, using 5-nm-thick Cr as a sticking layer. The Au traces in the CPS are measured under an optical microscope to be 20.4- $\mu\text{m}$  wide, with a 7.6- $\mu\text{m}$  gap in between.

We then transfer the GaAs switches onto the reserved spots in the CPS. The switches are fabricated using the method described in Ref. [1], and the transfer is performed using a polydimethylsiloxane (PDMS) stamp cured in a Si mold. The switches are placed such that their slanted sidewalls face the propagation direction of the CPS. Another round of photolithography and electron-beam evaporation is used to connect the switches to the CPS. Before metallization, we soak the chip in 20% HCl for 3 minutes to remove the oxidized surface layer of GaAs. A 180-nm Au layer is deposited from the top, and two 60-nm layers are deposited at 45° facing the two slanted sidewalls of GaAs to ensure robust connections. A 5-nm Cr sticking layer is used in each deposition.

The final step is to fabricate the narrowed section of the waveguide. The pattern, which is designed to gradually shrink the CPS width by a factor of 10 while keeping the width-to-gap ratio constant, is defined using electron-beam lithography (EBL). During the same write, a replica of the narrowest segment is defined roughly 1 mm away from the actual CPS. After Cr/Au metallization using electron beam evaporation, this replica is inspected using SEM and the metal width (gap) is determined to be 1.98  $\mu\text{m}$  (0.77  $\mu\text{m}$ ). This EBL/ metallization process is then repeated, with an unintentional 0.28  $\mu\text{m}$  offset (measured by AFM afterwards) along the vertical direction in Fig. S1, which results in a 245-nm thick pattern with a two-step sidewall profile as shown in Fig. 2b. These measured actual (instead of designed) geometries are then used in the simulations.

In all photolithography processes, we use a double-layer resist consisting of LOR5A (Microchem) and S1818 (Shipley). The developer and liftoff solvent are MF319 (Shipley) and Remover PG (Kayaku), respectively. For the EBL processes, we use a double-layer resist formed by 495 PMMA A4 and 950 PMMA A4 (Microchem). A layer of Spacer 300Z (Snowa Denko) is coated on top to prevent charging. The electron beam energy is 100 keV. The developer is iced isopropanol-water mixture with 3:1 volume ratio, and the liftoff solvent is acetone.

## 2. Measurements

All measurements are performed in a vacuum chamber with optical access, where the sample mount is cooled to a base temperature of 20 K using a closed cycle cryocooler (Advanced Research Systems).

For THz measurements, the output of a femtosecond fiber laser (Menlo Systems Orange, 1040 nm, 80 MHz) is frequency-doubled in a  $\beta$ -BaB<sub>2</sub>O<sub>4</sub> (BBO) crystal and used to excite the photoconductive switches. A 5X objective (Mitutoyo) is used to allow a large field of view covering both switches. All DC voltages are applied using Keithley 2614B source meters, while the AC monitoring voltage  $V_m$  is applied using a Rigol DG1022Z waveform generator. The delay modulation is implemented using a retroreflector mounted on a modulated translation stage (Thorlabs NF15AP25). The detector photocurrent is collected using a 1211 current preamplifier (DL instruments), and the lock-in measurements are performed using two SR830 lock-in

amplifiers (Stanford Research Systems). The Keithley source meters are also used to measure the resistance of ITO with a bias voltage not exceeding 10 mV.

For optical measurements, the same objective is used. A halogen lamp illuminates the entire sample, and a pin hole is used to filter out reflected light from a single spot in a confocal geometry. The selected beam is then collected by a home-built spectrograph with a thermoelectrically cooled camera (Pixis 100, Princeton Instruments). The objective is moved to access different spots on the sample.

### 3. Optical determination of $V_0$

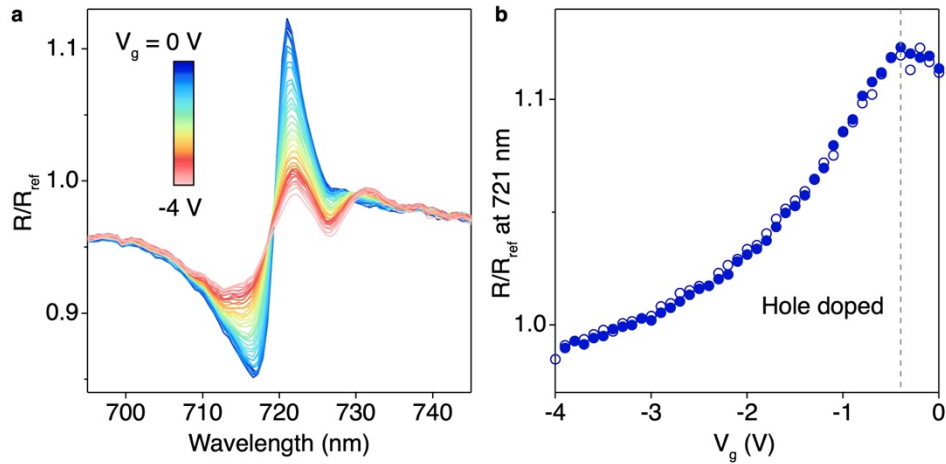


Fig. S2. Optical characterization of sample. **a.** Reflectance ( $R$ ) of  $\text{WSe}_2$  at different gate voltages  $V_g$ , normalized by that of  $\text{hBN}$  without  $\text{WSe}_2$  ( $R_{\text{ref}}$ ). Data collected in 0.1 V steps. **b.**  $R/R_{\text{ref}}$  at 721 nm as a function of  $V_g$ . Open and closed circles represent data measured with decreasing and increasing  $V_g$ , respectively. As marked by the dashed vertical line, hole doping happens below -0.4 V without notable hysteresis.

For gated regions of  $\text{WSe}_2$  not covered by the CPS, the onset voltage for hole doping  $V_0$  can be determined using optical measurements [2]. Fig. S2 shows the evolution of the A exciton resonance in  $\text{WSe}_2$  as a function of  $V_g$ . With decreasing  $V_g$ , the peak at 721 nm begins to drop at -0.4V, indicating the onset of hole doping. We have checked a few spots on the sample and the variation of  $V_0$  is around 0.1 V.

### 4. ITO sensing of $\text{WSe}_2$ doping state

From ITO test samples sputtered on  $\text{SiO}_2/\text{doped Si}$  chips, we have learned that (1) the contact resistance between ITO and Cr/Au is negligible in comparison with the ITO sheet resistance, and (2)  $\sigma_{\text{ITO}}$  changes linearly with gate voltage (applied to the Si backgate in these tests) and thus carrier density when the gating-induced density change  $\Delta n_{\text{ITO}} \ll n_{\text{ITO}}$ .

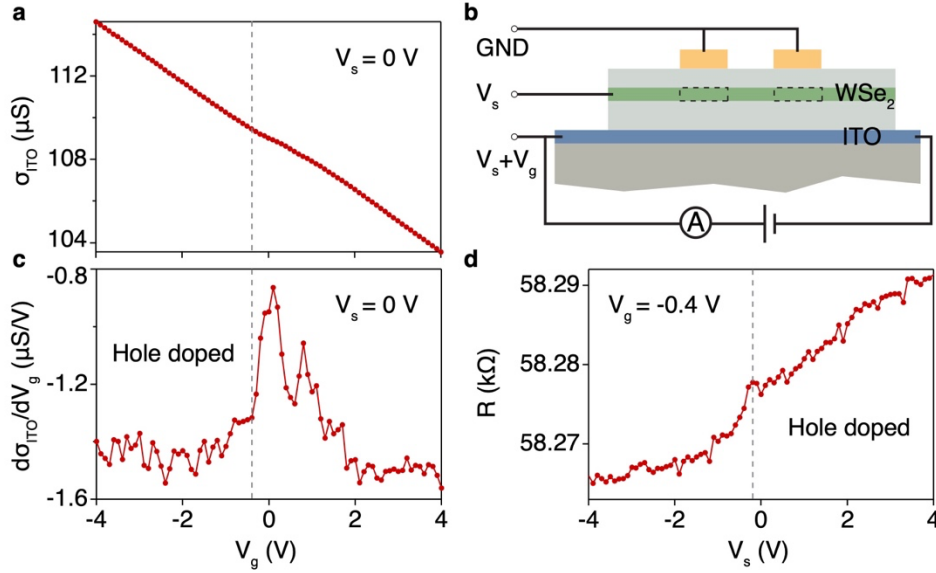


Fig. S3. ITO sensing. **a**. Sheet conductance of ITO in the region overlapping with WSe<sub>2</sub> as a function of  $V_g$ .  $V_s$  is fixed at 0 V during measurement. Data are converted from two-terminal resistance measurements according to the geometry illustrated in Fig. S1. As the waveguide traces are much narrower than the full overlapping region, effects from the dual-gated regions are ignored. **b**. Schematic of the resistance measurement. The dual-gated regions in WSe<sub>2</sub> are highlighted by the dashed rectangles with exaggerated width. **c**. Derivative of the data in **a** with respect to  $V_g$ . The change of slope in  $\sigma_{\text{ITO}}$  at -0.4 V (vertical dashed line) indicates that the chemical potential of WSe<sub>2</sub> is swept across its valence band edge. **d**. Two-terminal resistance of ITO ( $R$ ) as a function of  $V_s$ .  $V_g$  is fixed at -0.4 V during measurement. The change of slope at -0.2 V (vertical dashed line) indicates that the chemical potential of WSe<sub>2</sub> is swept across its valence band edge in the dual-gated regions. During measurements, we observe a slow and constant drift of  $R$  with time, likely because of oxygen loss in ITO in vacuum. Nevertheless, the drift is small, and its effect is further suppressed by averaging many back-and-forth scans.

Utilizing these effects, we can determine the onset of hole doping in WSe<sub>2</sub> by measuring the two-terminal resistance of ITO ( $R$ ) in the actual device. For large negative  $V_g$  values, the WSe<sub>2</sub> is hole doped and the sheet conductance of ITO changes linearly with  $V_g$  (Fig. S3a) as expected. A mobility  $\mu_{\text{ITO}} \approx 40 \text{ cm}^2\text{V}^{-1}\text{s}^{-1}$  is estimated from the slope. With increasing gate voltage, the slope changes at -0.4 V (Fig. S3c), indicating that the chemical potential of WSe<sub>2</sub> leaves the valence band. This onset voltage agrees with the value extracted from the optical measurements in Fig. S2.

To determine the  $V_s$  that aligns the WSe<sub>2</sub> hole density in the dual-gated region (dashed rectangles in Fig. S3b) with the rest of the sample, we fix  $V_g$  at -0.4 V and measure  $R$  as a function of  $V_s$  (Fig. S3d). For large positive  $V_s$  values where the WSe<sub>2</sub> is hole doped, a constant slope is observed. With decreasing  $V_s$ , a change of slope happens at -0.2 V. This indicates that the chemical potential of WSe<sub>2</sub> enters its bandgap, such that more electric field acts on the ITO backgate instead. Thus, by fixing  $V_s$  at -0.2 V and sweeping  $V_g$ , the hole densities beneath the

waveguide and in the rest of the gated region are approximately aligned in the THz measurements.

### 5. Effect of $V_g$ -dependent $\sigma_{\text{ITO}}$ on measuring sample conductivity

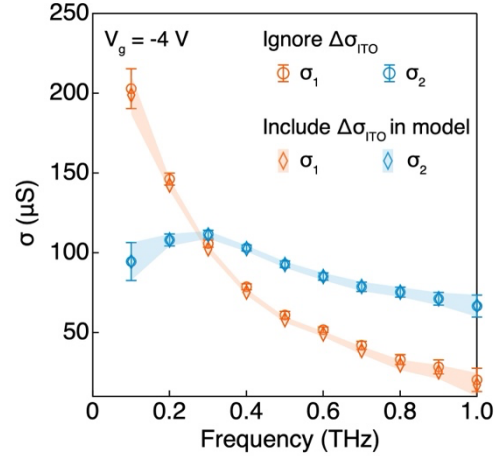


Fig. S4. Comparison of WSe<sub>2</sub> conductivity  $\sigma$  obtained using two different mappings between  $t/t_0$  and  $\sigma$ . Circles: the change of  $\sigma_{\text{ITO}}$  with  $V_g$  ( $\Delta\sigma_{\text{ITO}}$ ) is ignored during the calculation of the mapping. Diamonds:  $\Delta\sigma_{\text{ITO}}$  is included in calculation. The error bars and shaded regions represent 1- $\sigma$  error propagated from noise in measurements.

In the main text, we ignore the gate dependence of  $\sigma_{\text{ITO}}$  because it is much smaller than the gating-induced conductivity change in WSe<sub>2</sub>. This effect can also be included and compensated, by calculating  $t_0$  using the measured  $\sigma_{\text{ITO}}$  (Fig. S3a) at  $V_g = 0$  V and  $t$  using  $\sigma_{\text{ITO}}$  at the corresponding  $V_g$ . In Fig. S4 we compare the WSe<sub>2</sub> conductivity obtained through both treatments for  $V_g = -4$  V. Including the  $V_g$  dependence of  $\sigma_{\text{ITO}}$  results in a slightly smaller  $\sigma_1$ . Although the difference is minimal here, this compensation may become important for samples with lower mobilities.

### 6. Determine DC dielectric constant of hBN

We use a separate dual-gated graphene device to determine the DC dielectric constant of hBN (Fig. S5). The graphene is gated through a 32-nm-thick hBN flake by a Cr/Au electrode on the

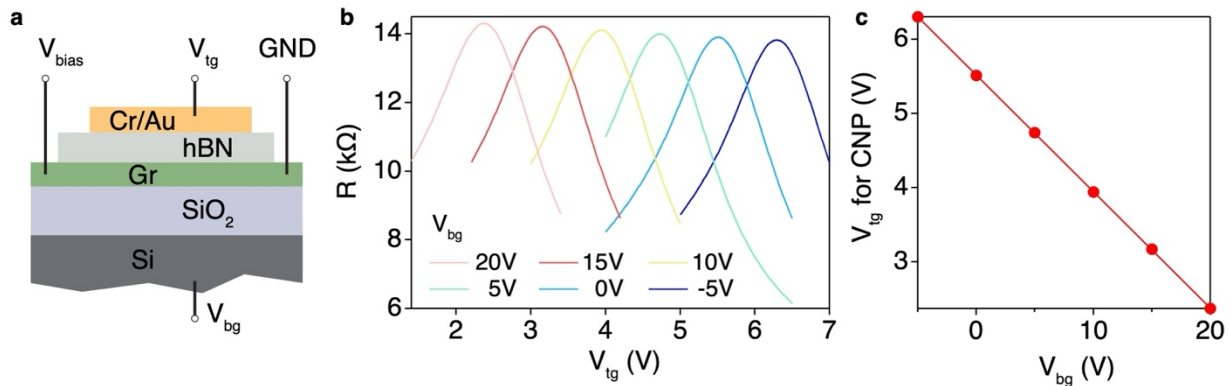


Fig. S5. Determine DC dielectric constant of hBN. **a**. Schematic of the dual-gated graphene (Gr) device. **b**. Two-terminal resistance ( $R$ ) of graphene as a function of topgate voltage ( $V_{\text{tg}}$ ) at different backgate voltage ( $V_{\text{bg}}$ ) values. The bias voltage ( $V_{\text{bias}}$ ) used in measurement is  $\pm 5$  mV. **c**. Circles: resistance peak positions in **b** as a function of  $V_{\text{bg}}$ . The red line is a linear fit to the data. CNP: charge neutral point.

top, and through  $285 \pm 20$  nm of thermal oxide by a doped-silicon substrate on the bottom. The hBN flake is obtained from the same batch of crystals used in the actual THz device. We measure the two-terminal resistance of graphene to determine the charge-neutral top gate voltage ( $V_{tg}$ ) at different back gate voltages ( $V_{bg}$ ). From the slope of  $V_{tg}$  at charge neutral as a function of  $V_{bg}$ , we determine the DC dielectric constant of hBN  $\epsilon_r = 2.8 \pm 0.3$  using a thermal oxide dielectric constant of 3.9.

## 7. Details of waveguide mode simulations

We use the ARPACK mode solver provided in COMSOL to solve the waveguide mode in each CPS segment. The center regions we simulate have sizes larger than  $400 \mu\text{m} \times 400 \mu\text{m}$ . They are surrounded by a perfectly matched layer to allow radiative loss. A symmetry condition is enforced to reduce the computation cost. Inside the center region, the metal traces are modeled as perfect conductors. In the sample segment, WSe<sub>2</sub> is treated as a boundary, where the surface current density equals to the product of in-plane electric field and sheet conductance. The thickness of WSe<sub>2</sub> is ignored, and its width is set to  $40 \mu\text{m}$ . As this width is much larger than the waveguide width, the detailed value does not affect the simulation result. The ITO is modeled in a similar way, with its width set to  $50 \mu\text{m}$ . The THz dielectric constants of hBN and quartz are set to 4.67 and 4.44 for the in-plane directions, and 4.20 and 4.64 for the out-of-plane direction, respectively [3,4]. Because these dielectric constants are close to each other, changing the width of hBN does not affect the results much, even in the segments where the waveguide width is large. Thus, for segments in which hBN flakes exist, their width is set to either  $80 \mu\text{m}$  (without ITO) or  $50 \mu\text{m}$  (with ITO).

To ensure that the correct mode is found, we have verified that the energy carried by the mode is concentrated near the metal traces, and the current along the propagation direction is negligible inside the sample and the ITO. We have also simulated situations where analytical expressions are available [5] and verified the correctness of results.

## References

- [1] P. Gallagher, C.-S. Yang, T. Lyu, F. Tian, R. Kou, H. Zhang, K. Watanabe, T. Taniguchi, and F. Wang, Quantum-critical conductivity of the Dirac fluid in graphene, *Science* 364, 158 (2019).
- [2] E. C. Regan, D. Wang, C. Jin, M. I. Bakti Utama, B. Gao, X. Wei, S. Zhao, W. Zhao, Z. Zhang, K. Yumigeta, M. Blei, J. D. Carlström, K. Watanabe, T. Taniguchi, S. Tongay, M. Crommie, A. Zettl, and F. Wang, Mott and generalized Wigner crystal states in WSe<sub>2</sub>/WS<sub>2</sub> moiré superlattices, *Nature* 579, 359 (2020).
- [3] A. J. Gatesman, R. H. Giles, and J. Waldman, Submillimeter optical properties of hexagonal boron nitride, *J. Appl. Phys.* 73, 3962 (1993).
- [4] M. Naftaly and A. Gregory, Terahertz and Microwave Optical Properties of Single-Crystal Quartz and Vitreous Silica and the Behavior of the Boson Peak, *Appl. Sci.* 11, 6733 (2021).
- [5] R. N. Simons, *Coplanar Waveguide Circuits, Components, and Systems*, 1st ed. (Wiley, 2001).